

A PRIMER ON UNIFYING DEBRIS DISK MORPHOLOGIES

EVE J. LEE¹, EUGENE CHIANG^{1,2}
Draft version November 9, 2018

ABSTRACT

A “minimum model” for debris disks consists of a narrow ring of parent bodies, secularly forced by a single planet on a possibly eccentric orbit, colliding to produce dust grains that are perturbed by stellar radiation pressure. We demonstrate how this minimum model can reproduce a wide variety of disk morphologies imaged in scattered starlight. Five broad categories of disk shape can be captured: “rings,” “needles,” “ships-and-wakes,” “bars,” and “moths (a.k.a. fans),” depending on the viewing geometry. Moths can also sport “double wings.” We explain the origin of morphological features from first principles, exploring the dependence on planet eccentricity, disk inclination dispersion, and the parent body orbital phases at which dust grains are born. A key determinant in disk appearance is the degree to which dust grain orbits are apsidally aligned. Our study of a simple steady-state (secularly relaxed) disk should serve as a reference for more detailed models tailored to individual systems. We use the intuition gained from our guidebook of disk morphologies to interpret, informally, the images of a number of real-world debris disks. These interpretations suggest that the farthest reaches of planetary systems are perturbed by eccentric planets, possibly just a few Earth masses each.

Subject headings: Fomalhaut, HR 4796A, HD 15115, HD 15745, HD 32297, HD 61005, HD 106906, HD 157587, HD 181327

1. INTRODUCTION

Orbiting stars $\gtrsim 10$ Myr old, “debris disks” are thought to trace the aftermath of planet formation (for a review, see Wyatt 2008). By definition, they are composed of optically thin dust grains, generated from the collisional attrition of larger parents. Observations of debris disks shed light on the size distribution and velocity dispersion of constituent bodies (e.g., Shannon & Wu 2011; Pan & Schlichting 2012; and references therein), and by extension the processes by which planetesimals and planetoids build up and grind down. Debris disks may also serve as signposts for embedded planets (e.g., Mouillet et al. 1997; Rodigas et al. 2014; Nesvold et al. 2016; and references therein).

The morphologies of debris disks are coming into increasingly sharp resolution with the advent of extreme adaptive optics instruments, including the *Gemini Planet Imager* (*GPI*; Macintosh et al. 2014), *SPHERE* (Beuzit et al. 2008), and *SCEXAO* (Jovanovic et al. 2015). In past and present observing campaigns, a variety of disk shapes have been uncovered, some featuring warps (e.g., Heap et al. 2000; Apai et al. 2015; Millar-Blanchaer et al. 2015; Wang et al. 2015) and eccentric rings (e.g., Kalas et al. 2005; Wahhaj et al. 2014; Perrin et al. 2015), and others evoking “moths” (e.g., Hines et al. 2007; Maness et al. 2009; Ricarte et al. 2013) and “needles” (e.g., Kalas et al. 2007b, 2015). Some imaged features have even been observed to vary with time (Boccaletti et al. 2015). Schneider et al. (2014) present a beautiful compilation of debris disk images taken with the *Hubble Space Telescope* (*HST*).

Disk structures that are non-axisymmetric are es-

pecially intriguing because they hint at gravitational sculpting by planets (assuming disk self-gravity is negligible; see, e.g., Jalali & Tremaine 2012 for a contrarian view). Foundational work was done by Wyatt et al. (1999), who calculated how one or more planets on eccentric, inclined orbits imprint ellipticities and warps onto debris disks. The planetary perturbations treated by these authors are secular, i.e., orbit-averaged in the sense that the gravitational potential presented by each planet is that of a smooth, massive wire (see also the textbook by Murray & Dermott 2000). Mean-motion commensurabilities with a planet can also shape disks by truncating them in a chaotic zone of overlapping first-order resonances (e.g., Wisdom 1980; Quillen 2006; Pearce & Wyatt 2014; Nesvold & Kuchner 2015b). Individual resonances can also, in principle, trap disk particles and clump them azimuthally (e.g., Kuchner & Holman 2003; Stark & Kuchner 2009). Such resonant clumps, moving at pattern speeds that typically differ from local Kepler frequencies, have yet to be confirmed in extrasolar debris disks. The preponderance of evidence shows that debris disks are smooth (e.g., Hughes et al. 2012), suggesting that secular effects dominate their appearance.

We offer here a systematic exploration of the morphologies of planet-perturbed debris disks, as imaged in scattered starlight. We focus on what is arguably the simplest possible scenario: a narrow ring of parent bodies forced secularly by a single planet, producing dust grains that are propelled outward by stellar radiation pressure. Our work builds on Wyatt et al. (1999) by supplying synthetic scattered light images of disks viewed from all possible directions. For all its simplicity, the model contains a surprisingly large variety of morphologies, and we will assess, in a qualitative way, the extent to which the observed real-world diversity of shapes (rings, flares, moths, needles, and the like) may be attributed to differences in viewing geometry; in other words, we explore

¹ Department of Astronomy, University of California Berkeley, Berkeley, CA 94720-3411, USA; evelee@berkeley.edu, echiang@astro.berkeley.edu

² Department of Earth and Planetary Science, University of California Berkeley, Berkeley, CA 94720-4767, USA

a “unification” model for debris disks, by analogy with unification models for active galactic nuclei. We do not expect our model to be able to explain every detail of resolved disk images, but submit our work as a starting point for interpreting those images: a baseline reference that can guide more sophisticated theories.

Our paper is straightforward. After describing the model elements and computational procedure (Section 2), we present synthetic scattered light images (Section 3) and compare them informally to actual systems (Section 4). Our aim is to provide a primer on debris disk morphology: to explain features from first principles, and develop intuition for mapping scattered light observations to the underlying parent disks and attendant planets. This paper is intended as a more general expansion of ideas discussed by Esposito et al. (submitted) to explain the moth-like morphology presented by HD 61005 (see also Fitzgerald et al. 2011 for the original proposal).

2. MODEL

We posit a planet of mass $M_{\text{planet}} = 10M_{\oplus}$ on an orbit with semi-major axis $a_{\text{planet}} = 30$ AU and eccentricity $e_{\text{planet}} \in (0, 0.25, 0.7)$ about a star with mass $M_* = 1M_{\odot}$. The planet’s orbit lies in the reference (x - y) plane, with its longitude of periape $\varpi_{\text{planet}} = 0$ (the planet’s periape is located on the x -axis).

Debris disk bodies are of two kinds: parent bodies and dust particles. The latter are spawned from the former. Parent bodies (subscripted p) are located exterior to the planet’s orbit and number $N_p = 1000$ in all. They have semi-major axes distributed uniformly from just outside the planet’s chaotic zone (Wisdom 1980; Quillen 2006; Quillen & Faber 2006; Chiang et al. 2009; Nesvold & Kuchner 2015b),

$$a_{p,\text{inner}} = a_{\text{planet}} \left[1 + 2(M_{\text{planet}}/M_*)^{2/7} \right], \quad (1)$$

to a value 10% larger,

$$a_{p,\text{outer}} = 1.1a_{p,\text{inner}}. \quad (2)$$

Thus our debris disks are really debris rings, as inspired by the narrow belts observed in, e.g., HR 4796A, Fomalhaut, AU Mic, and the Kuiper belt. For the highest value of $e_{\text{planet}} = 0.7$ that we consider, equation (9) of Pearce & Wyatt (2014) is more accurate and gives a value for $a_{p,\text{inner}} - a_{\text{planet}}$ that is ~ 2 times larger than the one predicted by our equation (1); we neglect this correction for simplicity.

A parent body’s eccentricity vector — a.k.a. its Runge-Lenz vector, which points toward periape and has a length equal to the eccentricity — is the vector sum of its forced and free eccentricities (e.g., Murray & Dermott 2000). The forced eccentricity vector is computed from Laplace-Lagrange (L-L) secular theory; in the one-planet case which we are considering, the forced vector points parallel to the planet’s eccentricity vector (i.e., in the positive x -direction), and has a magnitude specific to the body’s orbital semi-major axis:

$$e_{p,\text{forced}} = \frac{b_{3/2}^{(2)}(a_{\text{planet}}/a_p)}{b_{3/2}^{(1)}(a_{\text{planet}}/a_p)} e_{\text{planet}}, \quad (3)$$

where the b ’s are the usual Laplace coefficients. As $a_{\text{planet}}/a_p \rightarrow 1$, $e_{p,\text{forced}} \rightarrow e_{\text{planet}}$. The components

of the free eccentricity vectors, as resolved in $(h, k) \equiv (e \sin \varpi, e \cos \varpi)$ space, are

$$h_{p,\text{free}} = e_{p,\text{free}} \sin \varpi_{p,\text{free}} \quad (4)$$

$$k_{p,\text{free}} = e_{p,\text{free}} \cos \varpi_{p,\text{free}} \quad (5)$$

where $\varpi_{p,\text{free}}$ is a uniform deviate between 0 and 2π rad, and $e_{p,\text{free}}$ is a uniform deviate that extends from 0 to 0.02. The value of $e_{p,\text{free}}$ measures the random velocity dispersion, which in turn depends on how bodies collide and are gravitationally stirred (processes not modeled here; see, e.g., Pan & Schlichting 2012). Total parent body eccentricities are such that no parent body crosses the planet’s orbit; see Chiang et al. (2009) for numerical N -body integrations verifying orbital stability for parameters similar to those used here. That $\varpi_{p,\text{free}}$ ranges uniformly from 0 to 2π assumes that parent bodies are secularly relaxed; for our chosen parameters (M_{planet} , a_{planet} , $a_{p,\text{inner}}$, $a_{p,\text{outer}}$), differential precession timescales across the parent ring are of order a couple of Myrs, shorter than typical debris disk ages of tens of Myrs. To summarize, the parent bodies occupy, in the mean, a narrow elliptical ring located just outside the planet’s elliptical orbit and apsidally aligned with it.³

Parent body inclination vectors, resolved in $(p, q) \equiv (i \sin \Omega, i \cos \Omega)$ space, where i is inclination and Ω is the longitude of ascending node, behave analogously to eccentricity vectors. For our one-planet case, the forced inclination vector is the zero vector: forced orbits are co-planar with the planet’s orbit. Therefore parent body inclination vectors equal their free values:

$$p_{p,\text{free}} = i_{p,\text{free}} \sin \Omega_{p,\text{free}} \quad (6)$$

$$q_{p,\text{free}} = i_{p,\text{free}} \cos \Omega_{p,\text{free}} \quad (7)$$

where $\Omega_{p,\text{free}}$ is a uniform deviate between 0 and 2π rad (this assumes the system is secularly relaxed; see above), and $i_{p,\text{free}}$ is a uniform deviate between 0 and 0.02 rad.

To launch dust particles (subscripted d) from parent bodies, we first randomly draw, for a given parent body’s orbit, $N_{\text{launch}} = 100$ true anomalies. These true anomalies mark the launch positions for dust grains; for simplicity, we draw the N_{launch} true anomalies from a uniform distribution (on the one hand, periastron may be favored for collisions because orbital velocities are higher there, but on the other hand, apastron may be favored because parent bodies spend more time there; we discuss the effects of different choices for the distribution of launch sites in Section 3). At every true anomaly, a dust particle orbit is created whose instantaneous velocity at that position matches the parent body’s instantaneous velocity, and whose radiation β — the ratio of the force of stellar radiation pressure to that of stellar gravity — is drawn randomly from a distribution to be given below. To quantify our statements so far, the orbital elements

³ The low-order Laplace-Lagrange (L-L) secular theory which we use is quantitatively inaccurate at high e_{planet} but should be qualitatively correct. Pearce & Wyatt (2014) find good correspondence between their N -body integrations and L-L theory for e_{planet} as high as ~ 0.8 , provided the planet’s orbit lies within $\sim 20^\circ$ of the parent disk, as it does for all our models.

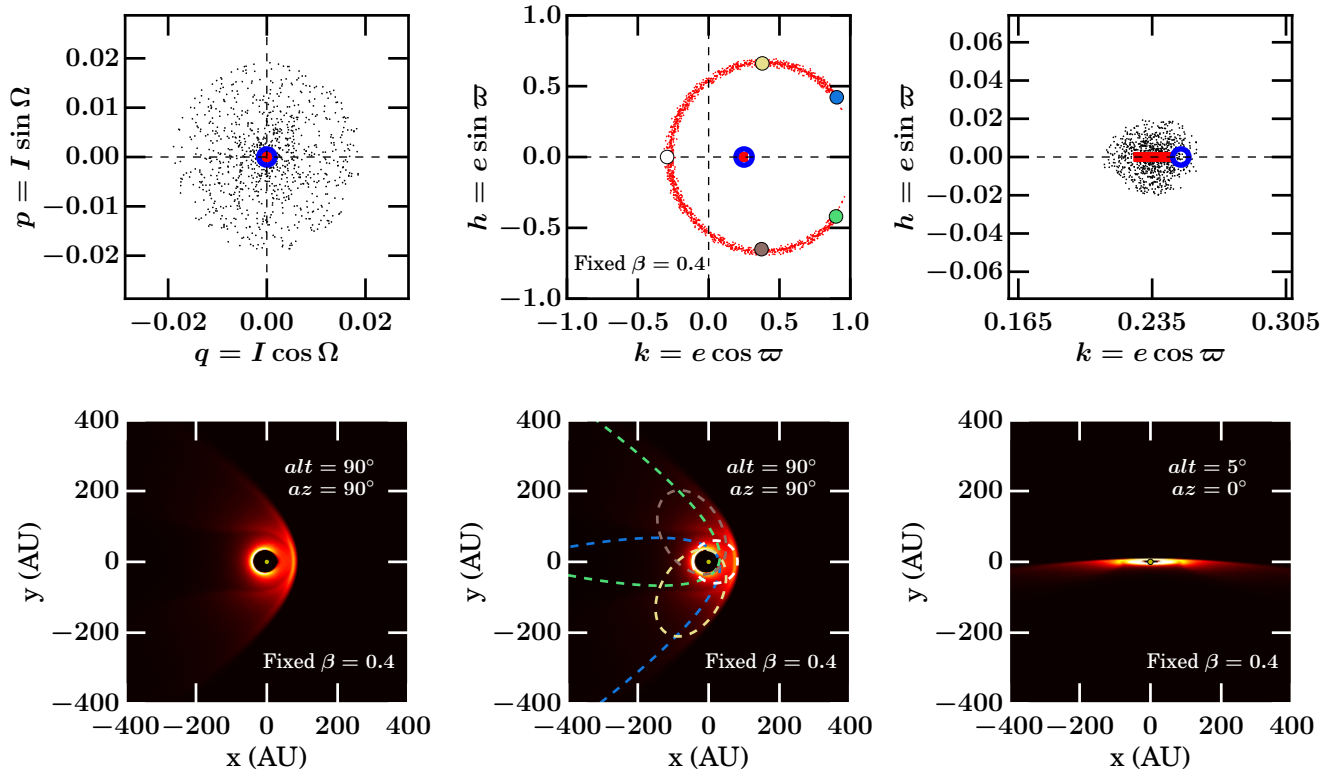


Figure 1. Elements of a sample model for which $e_{\text{planet}} = 0.25$, $\max e_{\text{p,free}} = \max i_{\text{p,free}} = 0.02$ (in radians), and — for this figure alone — a fixed $\beta = 0.4$ for dust particles. *Top row:* Inclination and eccentricity vector components of the planet (blue open circle), parent bodies (black points), and dust particles (red points). Forced eccentricities of parent bodies are shown as a red bar; full eccentricities differ from their forced values by up to $\max e_{\text{p,free}}$ (top right panel). Similarly, full inclinations differ from their forced values by up to $\max i_{\text{p,free}}$ (the half thickness of the disk). Because stellar radiation pressure does not alter orbital inclination, dust particle and parent body inclinations are identical (black points overlap red points in the top left panel). *Bottom row:* Synthetic scattered light images for this disk seen face-on ($alt = 90$ deg, bottom left and middle panels) and seen 5 deg above the planet’s orbital plane ($alt = 5$ deg, $az = 0$, bottom right panel). The scattered light features in the face-on (a.k.a. polar) view can be understood from an underlying “skeleton” of representative dust grain orbits, shown in matching colors in top and bottom middle panels. The nearly edge-on view in the right panel is such that the planet’s apocenter points toward the observer.

of each dust grain orbit are given by:

$$a_d = \frac{a_p(1 - e_p^2)(1 - \beta)}{1 - e_p^2 - 2\beta(1 + e_p \cos f_p)} \quad (8)$$

$$e_d = \frac{\sqrt{e_p^2 + 2\beta e_p \cos f_p + \beta^2}}{1 - \beta} \quad (9)$$

$$\omega_d = \omega_p + \arctan\left(\frac{\beta \sin f_p}{e_p + \beta \cos f_p}\right) \quad (10)$$

$$i_d = i_p \quad (11)$$

$$\Omega_d = \Omega_p \quad (12)$$

where ω is the argument of periape and f_p is the parent body’s true anomaly at launch.

The β -distribution is related to the assumed size distribution of dust grains. If the latter derives from a standard collisional cascade and obeys, e.g., a Dohnanyi distribution $dN/ds \propto s^{-7/2}$ for particle size s , then $dN/d\beta \propto \beta^{3/2}$, under the assumption that dust particles present geometric cross sections to radiation pressure ($\beta \propto 1/s$). But a conventional cascade underestimates the number of grains whose sizes are just shy of the radiation blow-out size. These grains are on especially

high-eccentricity and high-semi-major-axis orbits, avoiding interparticle collisions by spending much of their time away from the dense parent body ring. Their actual lifetimes against collisional destruction, and by extension their steady-state population, are underestimated by a standard cascade. We correct for this effect by scaling the number of dust grains in a given size bin to their orbital period P_d , which is longer at higher β . This same scaling is used by Strubbe & Chiang (2006, see their Figure 3) who show that it correctly reproduces the surface brightness profiles of collision-dominated debris disks like AU Mic. Our β -distribution therefore scales as

$$\begin{aligned} dN/d\beta &\propto \beta^{3/2} \times P_d \\ &\propto \beta^{3/2} \frac{(1 - \beta)^{3/2}}{[1 - e_p^2 - 2\beta(1 + e_p \cos f_p)]^{3/2}} \quad (13) \end{aligned}$$

where we have used $P_d \propto a_d^{3/2}$ and equation (8). The β -distribution extends from $\beta_{\text{min}} = 0.001$ to a maximum value β_{max} corresponding to a marginally bound (zero energy; $e_d = 1$) orbit. Each value of β_{max} is specific to a given launch position and velocity. The β -distribution given by (13) is very top-heavy; most grains have β near

the maximum value

$$\beta_{\max} = \frac{1 - e_p^2}{2(1 + e_p \cos f_p)}. \quad (14)$$

Along each dust particle orbit, we lay down, at random, $N_{\text{dust-per-orbit}} = 100$ dust particles. Their mean anomalies are uniformly distributed but their true anomalies are not; dust particles concentrate near apoapse, following Kepler’s equation. The dust particles, numbering $N_d = N_p \times N_{\text{launch}} \times N_{\text{dust-per-orbit}} = 10^7$ in all, are projected onto the sky plane of a distant observer and used to synthesize a scattered light image. The sky plane of 800×800 AU, centered on the star, is divided into 800×800 square cells, and each dust particle contributes, to the cell in which it is located, a surface brightness proportional to $\phi(g, \theta)/(\beta^2 r^2)$. Here $1/\beta^2$ accounts for the scattering cross section for each grain (assumed geometric), r is the distance between the dust particle and the host star, and $\phi(g, \theta)$ is the Henyey-Greenstein scattering phase function for asymmetry parameter $g = 0.5$ and θ equal to the angle between the dust particle and the observer with the vertex at the star. Multiple scattering of photons is neglected; this is a safe assumption insofar as debris disks are optically thin.

Figure 1 illustrates the basic ingredients of our model. It depicts how the locations of bodies in (p, q, h, k) space relate to one another, and to the resultant scattered light images, for a sample case $e_{\text{planet}} = 0.25$. For pedagogic purposes, and for Figure 1 only, we assign all dust particles a fixed $\beta = 0.4$, discarding particles not bound to the star. Surface brightness morphologies can be understood in terms of underlying dust particle orbits by starting from the face-on scattered light image (looking down the z -axis onto the x - y plane). The inner dust cavity is outlined by the launch sites of dust particles, i.e., the cavity rim coincides with the elliptical ring of parent bodies (the parent bodies themselves do not contribute to the scattered light image). Because launch velocities are “high” for the weakened gravitational potential felt by dust particles (the potential is weakened by $1 - \beta$), the cavity rim / parent body ring marks the periastra of dust particles. The bright half of the cavity rim, located on the negative x -axis, traces the periastra of $e \sim 0.3$ dust particles (drawn in white); these are launched from the apastras of their parents’ orbits. These same dust particles’ apastras form the “arc” located to the right of the cavity. The entire outer boundary of dust emission, of which the arc is the brightest segment, is demarcated by all the particle apastras. Particles with the largest eccentricities (e.g., yellow, blue, green, grey-brown), extending up to unity, are launched from near the periastra of their parents’ orbits, and form the barely visible “wings” extending above and below the arc. In a more edge-on view, these wings increase in brightness because of their increased line-of-sight optical depth. Viewed at 5 deg above the planet’s orbital plane, with the planet’s apoapse directed toward the observer, the wings appear downswep.

3. SYNTHETIC SCATTERED LIGHT IMAGES

Figures 2, 3, and 4 show the scattered light images for $e_{\text{planet}} = 0.25$, $e_{\text{planet}} = 0.70$, and $e_{\text{planet}} = 0$, respectively, with the radiation β following a distribution given

by (13). We smooth away some of the shot noise caused by a finite number of dust grains by convolving images (from Figure 2 onward) with a 2D Gaussian having a standard deviation of 2 pixels (2 AU). A side effect of the convolution is that it shrinks the dust inner cavity; we restore the cavity by masking out the corresponding pixels. The panels in each figure are computed from a variety of vantage points. The orientation of the observer (on the celestial sphere centered on the debris disk) is parametrized by altitude alt (inclination angle relative to the planet’s orbital plane; $alt = 0^\circ$ corresponds to the planet’s orbit seen edge-on, while $alt = 90^\circ$ gives a face-on view) and azimuth az (angle measured in the planet’s orbital plane; $az = 0^\circ$ corresponds to the apoapse of the planet’s orbit pointing toward the observer, while $az = 180^\circ$ directs the planet’s periapse toward the observer). For all images we rotate first in alt and then in az starting from $(alt, az) = (90^\circ, 0^\circ)$. We refer to Figures 2–4 as “alt-az” diagrams.

All three alt-az diagrams are displayed on a universal brightness scale. To bring out the fainter features, images are scaled to the square root of the surface brightness. More edge-on views have greater line-of-sight optical depths and therefore yield brighter disks. For reference, the angular half-thickness of our disk is $\max i_{p,\text{free}} = 0.02$ rad $\simeq 1^\circ$. Later in this section we will experiment with a thicker disk for which $\max i_{p,\text{free}} = 0.15$ rad $\simeq 9^\circ$.

In many of the views displayed in Figures 2–3, the eccentricity of the debris disk forced upon it by the eccentric planet manifests itself as a stellocentric offset: the star is displaced from the apparent geometric center of the ring’s inner cavity. Another signature of planet eccentricity is the tail of scattered light extending to one side of the star, seen most prominently for high e_{planet} . This tail arises from dust particles on high-eccentricity orbits launched from near the periastron of the parent body ring; in our diagnostic Figure 5, these orbits are color-coded green, white, and yellow (see in particular the bottom panels). High-eccentricity dust abounds as our β -distribution (13) is strongly weighted toward the maximum value just short of radiation blow-out. When this “sheet” of high- e dust particles is viewed just above its plane ($alt \sim 5$ – 10°) and in front of the star ($az = 0^\circ$), it appears in projection as a “fan” or “moth” whose wings sweep downward from the star. Higher planet eccentricities cause both the top and bottom boundaries of the fan to be more angled; compare the white contours in the leftmost panels of Figure 5. Maintaining the same above-the-plane view ($alt \sim 5$ – 10°), but now rotating the observer in azimuth so that the sheet of high-eccentricity dust is seen behind the star ($az = 180^\circ$), produces an up-swept fan (see Figures 2–3). Observer azimuths intermediate between 0° and 180° yield simultaneous top-down and left-right asymmetries. For example, comparing the left and right limbs of the disk seen at $az = 135^\circ$ and $alt = 10^\circ$ in Figure 3, we see that the left limb is more extended in length, has a lower peak brightness, and is angled more upward.

When the planet’s orbit is viewed nearly but not completely edge-on ($0^\circ < alt \leq 10^\circ$), with its periapse pointing toward the observer ($az > 90^\circ$), a faint “bar” emerges displaced from the star. This bar, seen below the star in Figures 2–3, is equivalent to the “arc” seen in front of the planet’s periastron in Figure 1; the bar/arc is comprised

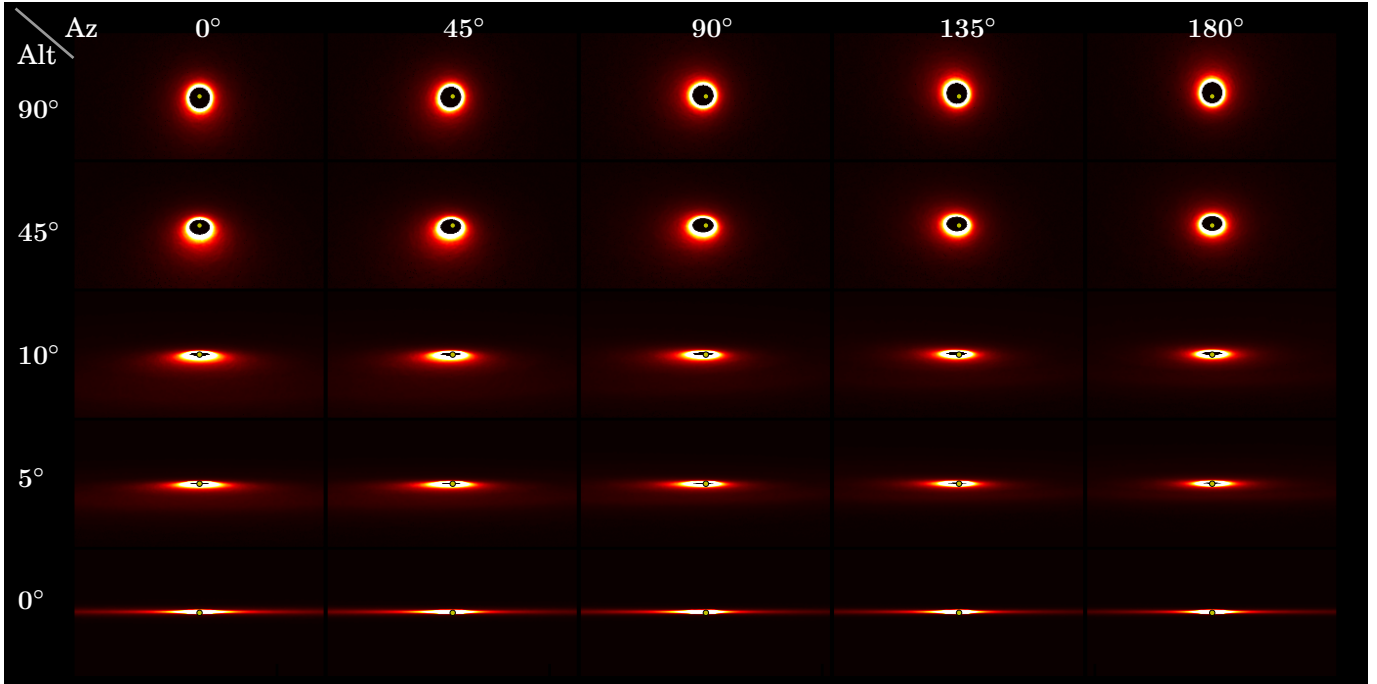


Figure 2. “Alt-az” diagram for the case $e_{\text{planet}} = 0.25$. Synthetic scattered light images of the debris disk are shown as a function of the observer’s altitude ($alt = 0^\circ/90^\circ$ gives an edge-on/pole-on view of the planet’s orbit) and azimuth ($az = 0^\circ/180^\circ$ has the planet’s apoapse/periapse pointing toward the observer). For this and other alt-az figures, we use an image scaling proportional to the square root of the surface brightness. Each alt-az snapshot is constructed from an $800 \text{ AU} \times 800 \text{ AU}$ grid, smoothed by convolving with a 2D Gaussian having a standard deviation of 2 AU, and truncated vertically to 400 AU. The convolution shrinks the dust inner cavity; we restore the cavity seen in the pre-smoothed image by masking out the corresponding pixels. The surface brightnesses of the brightest features are ~ 600 (10^4) times higher than that of the faintest features in the face-on (edge-on) view. The yellow dot in each panel marks the location of the central star.

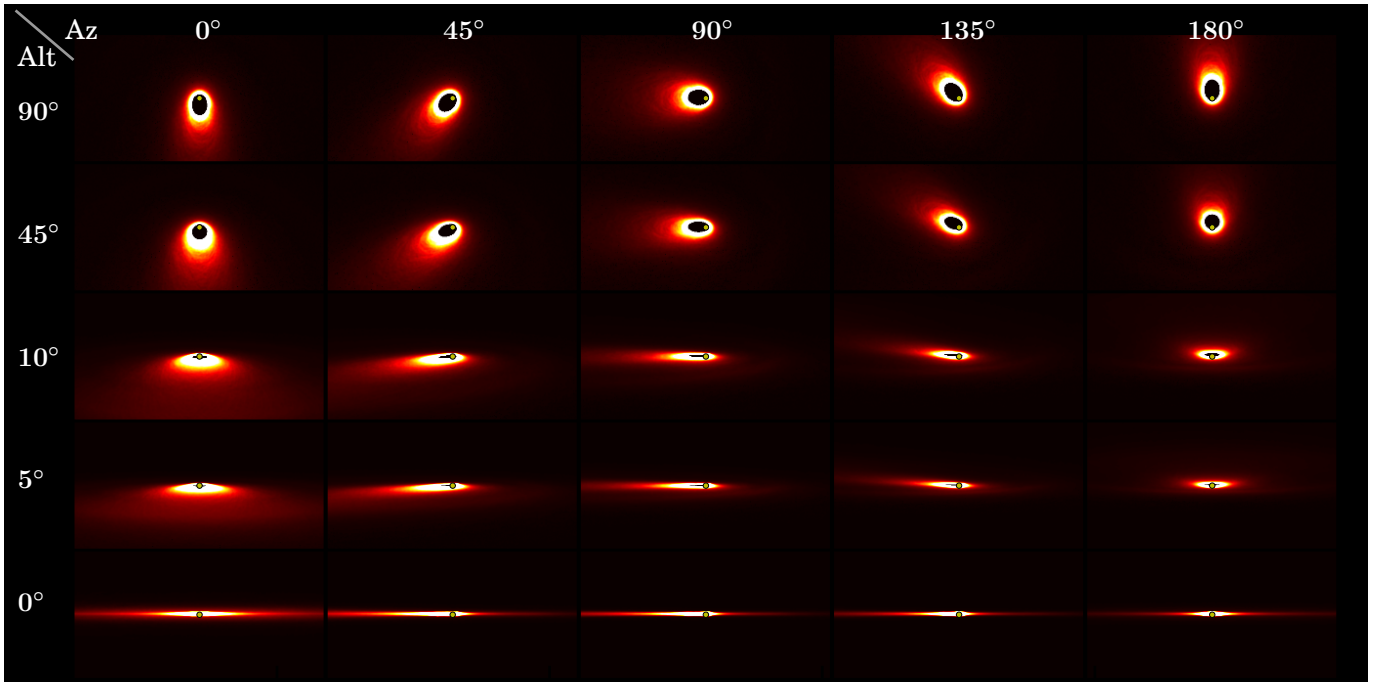


Figure 3. Same as Figure 2, but for a more eccentric planet with $e_{\text{planet}} = 0.7$. The surface brightnesses of the brightest features are $\sim 10^4$ (2×10^4) times higher than that of the faintest features in the face-on (edge-on) view.

of dust grains at their apastras, on orbits launched from near the apastras of their parent bodies. These orbits are apsidally anti-aligned relative the planet’s orbit (see the white orbit in Figure 1). The bar is brightest when seen

in forward-scattered light and at low observing altitudes which enhance its line-of-sight optical depth.

The above mentioned tail of scattered light extends only in the direction of the parent body disk’s apas-

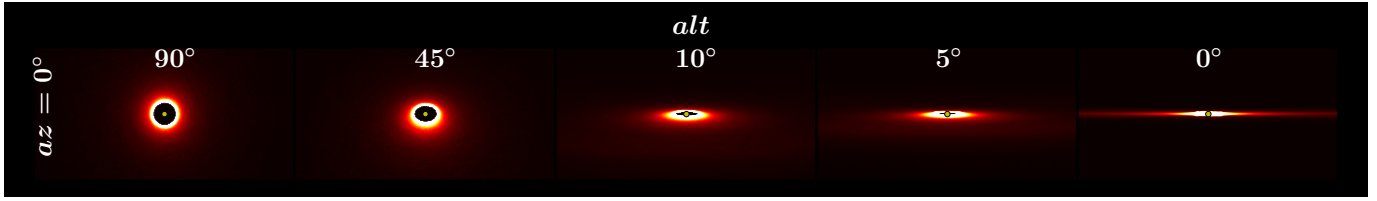


Figure 4. Same as Figure 2, but for $e_{\text{planet}} = 0$.

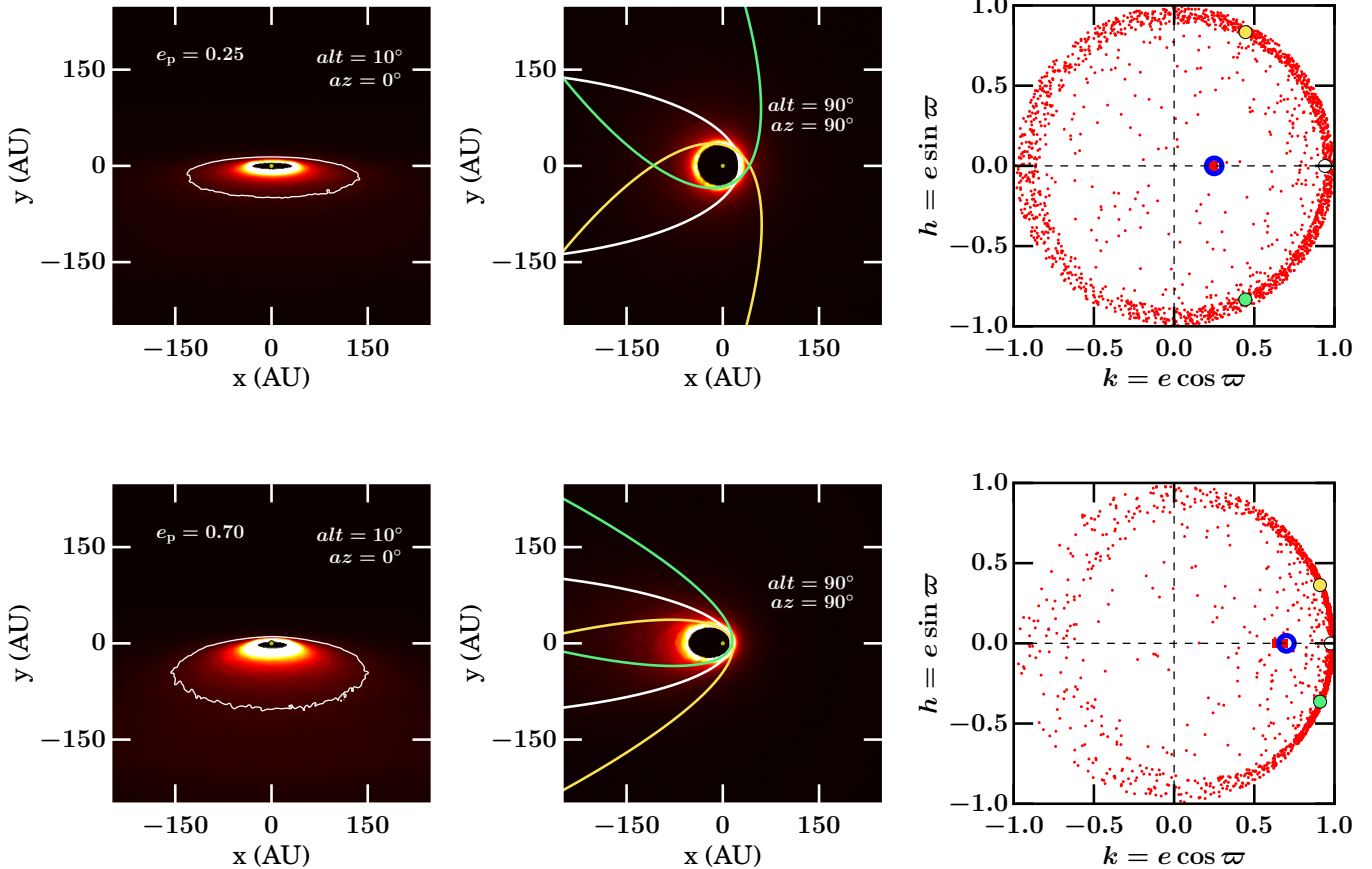


Figure 5. Zoomed-in images for $e_{\text{planet}} = 0.25$ (top row) and $e_{\text{planet}} = 0.7$ (bottom row). Left panels are nearly edge-on views ($alt = 10^\circ$), and are each overlaid with a contour of constant surface brightness. Middle panels are face-on views showing representative dust grain orbits, color-coded to correspond to the colored points in the right-hand h - k plots (whose remaining symbols have meanings identical to those in Figure 1). Note how most particles in h - k space cluster near unit eccentricity as a consequence of our top-heavy β -distribution (13). The white dust orbit is launched from parent body periastron, and the green and yellow dust orbits are chosen to have median eccentricities and longitudes of periastron. As planet eccentricity increases, increasingly many dust orbits have their periastra aligned with that of the planet, leading to a more extended and sharply angled “fan” of emission in nearly edge-on views.

tron (and by extension the planet’s apastron) because there are more dust grains on orbits apsidally aligned with their parents’ orbits than anti-aligned. This preference for apsidal alignment magnifies with increasing planet eccentricity, as shown in Figure 5, and can be understood as follows. For the simplifying case of coplanar orbits, dust grains have $0 \leq |\varpi_d - \varpi_p| < \pi/2$ if they are launched between a parent body’s periastron and its semi-minor vertex (where the semi-minor axis crosses the orbit). The range of true anomalies between periastron and the semi-minor vertex is greater than between the semi-minor vertex and apastron. This difference grows as e_{planet} grows; consequently, more dust grain orbits have $0 \leq |\varpi_d - \varpi_p| < \pi/2$ as e_{planet} increases.

The degree to which dust orbits apsidally align with the parent body ring depends not only on planet ec-

centricity, but also the distribution of parent body true anomalies at launch. Different distributions of launch sites are explored in Figure 6. Alignment is perfect — and the wings of the disk seen in projection are swept most strongly downward — if dust grains are launched exclusively from periastron (left panels). If instead launch mean anomalies are uniformly distributed — i.e., if launch true anomalies are weighted toward apastron where parent bodies linger — then apsidal alignment is weakened (right panels). Our standard model assumes a uniform distribution of launch true anomalies and represents an intermediate case (middle panels).

In the endmember case that all dust particles are launched at parent body periastra and have their orbits completely apsidally aligned, we can discern two sets of wings: a thin pair of wings sitting above a more diffuse

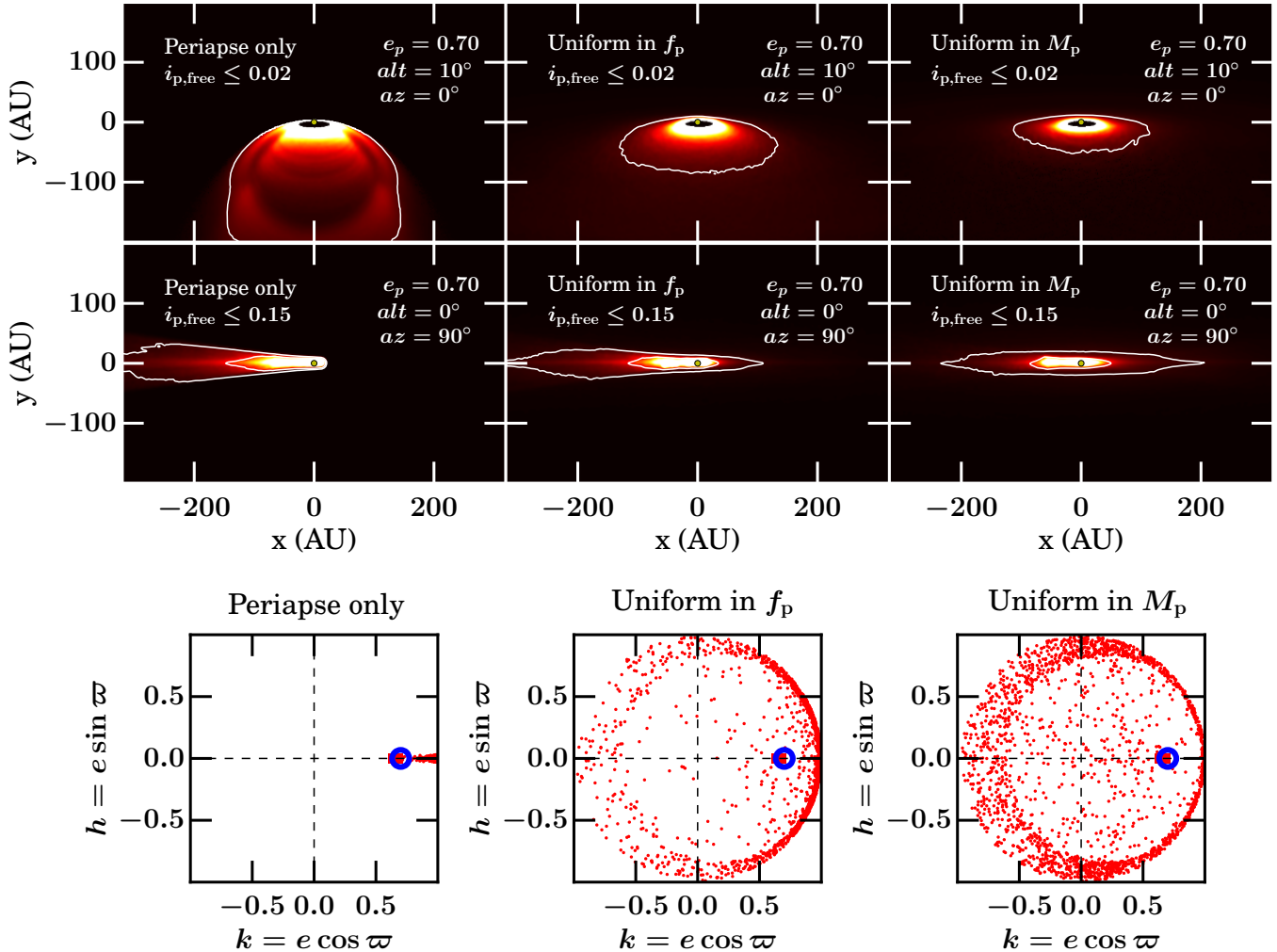


Figure 6. Experiments in the distribution of launch sites for dust particles, for the case $e_{\text{planet}} = 0.7$. If dust grains are launched strictly from the periastra of parent bodies, then all orbits are apsidally aligned (left column of panels; symbol meanings in the h - k plot are identical to those in Figure 1). If dust grains are launched at parent body mean anomalies M_p that are uniformly distributed between 0 and 2π , the preference for apsidal alignment is muted (right column of panels). Our standard model assumes that dust grains are launched at parent body true anomalies f_p that are uniformly distributed between 0 and 2π , and represents an intermediate case (middle column of panels). The top row displays corresponding scattered light images, observed at $alt = 10^\circ$ and $az = 0^\circ$ for our standard vertically thin disk with $\max i_{p,\text{free}} = 0.02$ rad. Each nearly edge-on disk, as traced by a white contour of constant surface brightness, resembles a “fan” or “moth”; the wings of the moth are angled more sharply downward as dust particle orbits are more strongly apsidally aligned (reading right to left). Note the “double winged moth” that appears when dust grains are launched exclusively from parent periastra (top left). The middle row features scattered light images observed at $alt = 0^\circ$ and $az = 90^\circ$ for a vertically thicker disk with $\max i_{p,\text{free}} = 0.15$ rad. The center panel features an inner “ship” surrounded by its “wake,” as detailed in the main text. Brightness asymmetries and vertical asymmetries across the ship-and-wake are magnified as dust grain launch sites concentrate toward parent body periastra (reading right to left).

and roughly parallel pair of wings below the star (top left panel of Figure 6). We can understand this “double wing” morphology using the face-on views shown in Figure 7. The upper set of wings seen in Figure 6 corresponds to the bright arc near periastron in Figure 7. This arc is especially luminous because of the confluence of orbits converging on nearly the same periastron. The lower set of wings in Figure 6 corresponds in Figure 7 to the pair of overdense “rays” located toward parent body apastron and symmetrically displaced above and below the apsidal line (the x -axis). These two local maxima in surface brightness — what look like a pair of jets spraying particles away from the star in the face-on view — arise from two effects: (1) the tendency of particles on a given orbit to be found closer to apoapse (where they linger) than to periape (which they zip through), and (2) the

lowering of the particle density along the apsidal line in the direction of apoapse, due to large orbit-to-orbit differences in apoapse distance — see the bottom panel of Figure 7. The broad distribution of apoapse distances (extending to infinity) is due in turn to a radiation- β distribution that abuts blow out. Effect (1) concentrates particles toward apoapse, while effect (2) dilutes the particle density along the apsidal line (in the direction of apoapse); the net effect is to concentrate particles at two orbital phases symmetrically displaced away from the apsidal line.

The difference between the “double wing” and the “bar” lies in their relative proximities to the central star. The outermost wing — what defines the edge of the disk — cuts almost directly across the star in projection, whereas the bar is necessarily displaced from the

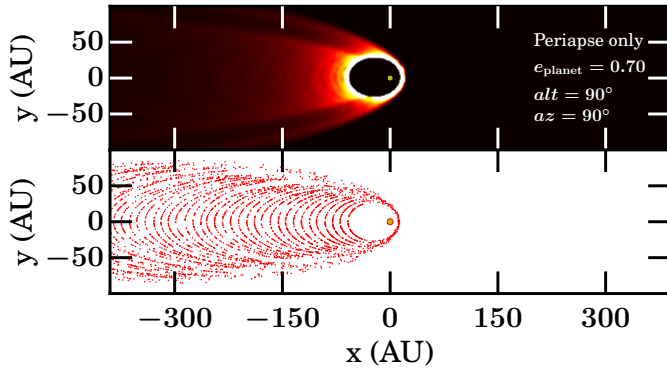


Figure 7. Understanding the origin of the double wings seen for some moths, as seen in the upper left panel of Figure 6 (see also the middle right panel of Figure 9 for another version of the double wing morphology). Double wings appear when all dust grains share practically the same periastron and apsidal line (x -axis) as a consequence of being launched only at parent body periastra. *Top:* Scattered light image of the same disk featuring double wings, but seen face on here. Emission near periastron generates the upper set of wings in Figure 6, while the pair of jet-like features displaced symmetrically above and below the apsidal line produces the lower set of wings. *Bottom:* Same as top, but plotting individual dust grains. Local overdensities generated at two orbital azimuths correspond to the two jets seen in the top panel.

star.

All of the behavior reported above persists if $\max i_{p,\text{free}}$ is increased from our standard value of 0.02 rad to 0.15 rad; i.e., the alt-az diagram for a vertically thicker disk looks similar to that of our standard thin disk. But there is more. Thickening the disk, and viewing it edge-on ($\text{alt} = 0^\circ$) and near quadrature ($45^\circ \leq \text{az} \leq 135^\circ$), reveals new morphological features, as seen in Figure 8. The disk’s outer isophote has a front (toward planet periastron) that is vertically thinner than its back, resembling the “wake” of a “ship” (inner isophote enclosing the dust cavity rim seen in projection). The head of the ship and the back of its wake comprise dust on orbits that are highly eccentric and closely apsidally aligned with the parent disk (these are represented by the white, green, and yellow orbits in Figure 5). Conversely, the stern of the ship and the front of its wake coincide with the few dust orbits that are anti-aligned with the parent disk and less eccentric. The wake grows in vertical thickness from front to back because the front is composed of dust at the apastron of low eccentricity orbits, while the back is composed of dust at the more distant apastron of high eccentricity orbits; at fixed inclination dispersion, the more distant apastron have greater heights above the disk midplane. As was the case for the moth (see above), the degree of vertical asymmetry for the wake depends on the distribution of dust grain launch sites: the more the launch sites concentrate near periastron, the more severe the asymmetry (see middle row of Figure 6).

4. SUMMARY AND DISCUSSION

We have explored in this work what a “minimum model” of a debris disk looks like in scattered light. The minimum model consists of a narrow ring of parent bodies, secularly perturbed by a single, possibly eccentric planet, producing dust grains whose orbits are made arbitrarily eccentric by stellar radiation pressure. The model has obvious relevance to systems like Fomalhaut and HR 4796A which patently feature narrow elliptical

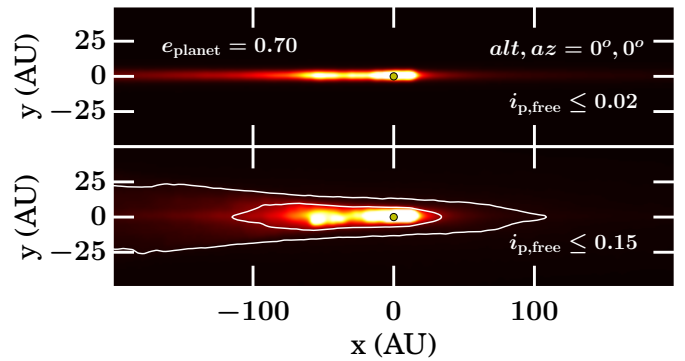


Figure 8. A sufficiently thick disk ($\max i_{p,\text{free}} = 0.15$ rad; bottom panel) seen edge-on features a “ship” (inner white contour of constant surface brightness) and its surrounding “wake” (outer white contour). The ship’s front/bow (on the positive x -axis, aligned with the underlying planet’s periastron) is brighter than its back/stern. The outer wake is narrower at its front than its back. The ship-and-wake morphology might be relevant for HD 106906; see Section 4.

rings.⁴ What might not be so obvious is that the minimum model can also help to explain many other morphologies documented in resolved images of debris disks — all by simple changes in viewing perspective. A message emerging from our work is that the outskirts of planetary systems are shaped by eccentric planets, possibly just a few Earth masses each.

In Figure 9 we summarize the various disk shapes that are possible. We classify these into five types: “ring,” “moth,” “bar,” “needle,” and “ship-and-wake.” The first four shapes can be generated even by a disk that is completely flat. We review each of these morphologies in turn, highlighting potential applications to observed systems, and close by listing future modeling directions.

4.1. “Ring”

Dust that is generated from an eccentric ring of parent bodies appears as an eccentric ring itself when viewed close to face on (top left panel of Figure 9). The inner rim of the ring is illuminated by dust particles near their periastra, while a skirt of diffuse emission extends outward from dust grains en route to their apastron. Some real-life examples of rings with offset host stars are provided by Fomalhaut (e.g., Kalas et al. 2005, their Figure 1), HR 4796A (e.g., Schneider et al. 2009, their Figure 3; Thalmann et al. 2011, their Figure 1; Perrin et al. 2015, their Figure 8; Grady et al. 2016), HD 181327 (e.g., Schneider et al. 2014, their Figure 33), and HD 157587 (Padgett & Stapelfeldt 2016; Millar-Blanchaer et al., submitted). These systems also feature diffuse emission exterior to their rings.

4.2. “Moth”

When the parent body ring is viewed nearly but not completely edge-on, with its apoapse pointing out of the sky plane toward the observer, a shape like a fan or moth materializes (top right panel of Figure 9). The resemblance of this morphology to the actual “Moth” (HD 61005; Hines et al. 2007) was first pointed out by Fitzgerald et al. (2011) and explored with detailed and quantita-

⁴ Perrin et al. (2015) suggest that the HR 4796A disk may be slightly optically thick.

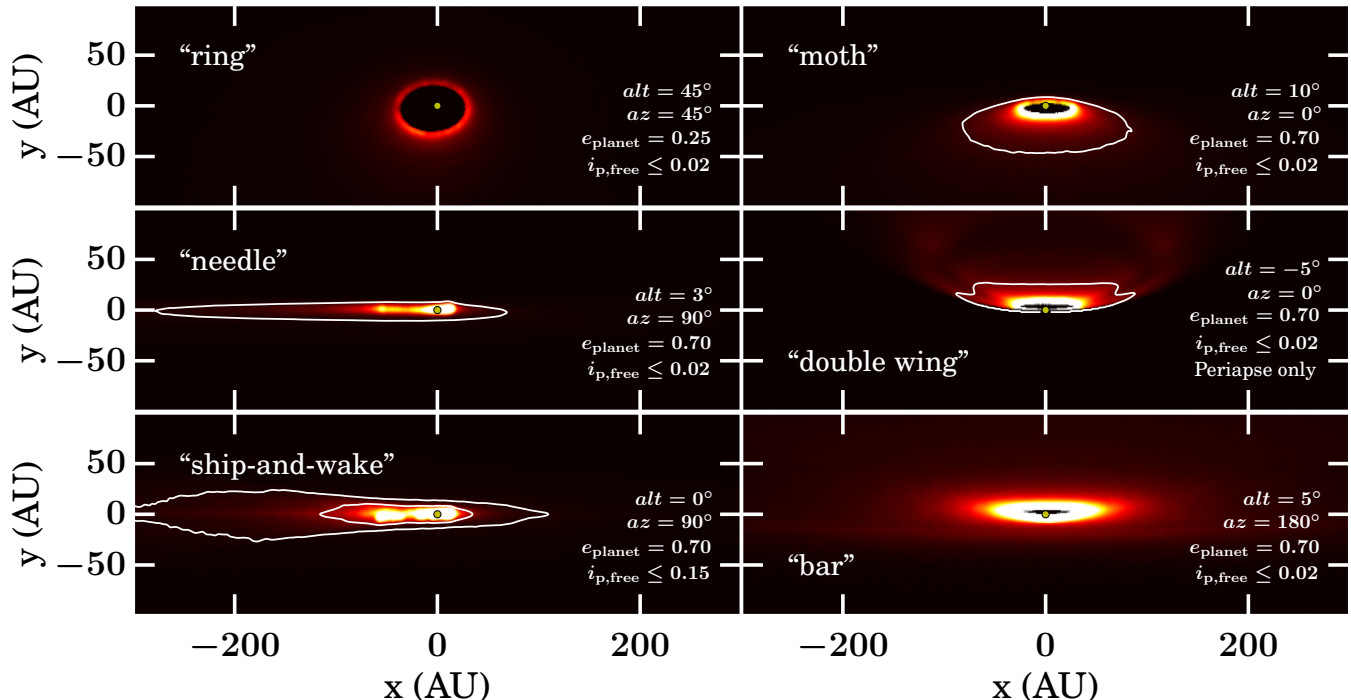


Figure 9. Prototypical debris disk morphologies seen in scattered light, as captured by a “minimum model” (single eccentric planet + ring of parent bodies + dust grains + stellar radiation pressure). Possible observable shapes include a “ring” (top left), a “needle” (middle left; this is essentially a ring seen edge-on), and a “ship-and-wake” (bottom left; this is basically a needle which is fat enough to resolve vertical structure). Right panels feature various kinds of “moths,” either our standard version where most dust grains are in front of the star and therefore appear bright in forward-scattered light (top right), a moth with “double wings” where dust grain orbits are perfectly apsidally aligned as a consequence of assuming that grains are launched exclusively from parent body periastra (middle right), and a “reverse moth” where most grains are behind the star, accompanied by a “bar” in front of the star (bottom right). Note the sharp wingtips seen in the “double wing” panel; this model looks encouragingly similar to HD 32297 (Schneider et al. 2014, their Figure 19b). The surface brightness contrasts between the brightest and the faintest features are ~ 36 , ~ 900 , $\sim 10^4$, ~ 260 , ~ 620 , and ~ 400 for the ring, needle, ship-and-wake, moth, double wing, and bar, respectively. The head of the ship is $\sim 400\times$ brighter than its stern. In the double wing, the two wings are $\sim 4\times$ brighter than the gap between them. The bar is $\sim 20\%$ brighter than the gap that separates it from the main disk.

tive models fitted to the Moth by Esposito et al. (submitted). For sample images of HD 61005, see, e.g., Figure 3 of Hines et al. (2007); Figure 1 of Maness et al. (2009); Figure 1 of Buenzli et al. (2010); and Figure 1 of Ricarte et al. (2013). The wings of our model moth are composed of dust grains on highly eccentric orbits that are apsidally aligned with the parent ring (and by extension the planet), and whose apastras are directed toward the observer. Viewing these grains from slightly above their orbital plane produces downswept wings; viewing them from below produces upswept wings (flip the top right panel of Figure 9 about the y -axis). If instead these grains’ apastras are directed into the sky plane away from the observer, then the wings of the moth appear foreshortened because most of the starlight is forward-scattered away from the observer (this is the “reverse moth” featured in the bottom right panel of Figure 9; the foreshortening is not apparent because the panel is made using a low contrast to highlight another feature, the “bar,” which will be discussed below). Note that the moth morphology does not depend on a non-zero inclination between the parent body ring and the planet; a perfectly flat system suffices, provided it is viewed slightly away from edge-on.

The degree to which the wings of the moth are angled depends on the degree to which dust grain orbits are apsidally aligned. In turn, the preference for apsidal alignment depends on both planet eccentricity and

the orbital phases at which parents give birth to dust grains. If dust grains are launched from parent body periastra and no other orbital phase, then the system is, in a sense, maximally non-axisymmetric; there is a “preferred” direction in space; apsidal alignment is perfect, and the moth wings sweep most strongly away from the horizontal. The wings of HD 61005 are angled by ~ 23 degrees from the horizontal (Buenzli et al. 2010; Esposito et al., submitted), suggesting high planet eccentricity and a strong preference for launching dust grains near parent periastra.

Another moth-like system is presented by HD 32297. Intriguingly, HD 32297 sports a second, fainter pair of moth wings that roughly parallel the first, as imaged by *HST* on scales of several arcseconds (e.g., Schneider et al. 2014, their Figures 18 and 19). Our minimum model can reproduce this “double wing” structure (middle right panel of Figure 9). When dust orbits are closely apsidally aligned, a first set of wings (closest to the star, toward the bottom of the panel) traces particles at and around their periastra, while another fainter set of wings (farther from the star, toward the top of the panel) is generated by particles near, but not at, their apastras. We can even try to make a connection to the disk geometry as revealed on smaller, subarcsecond scales at infrared wavelengths. Figure 4 of Esposito et al. (2014) (see also Figure 1 of Currie et al. 2012) reveals the emission closest to the star to be concave down (when north-west is up) and

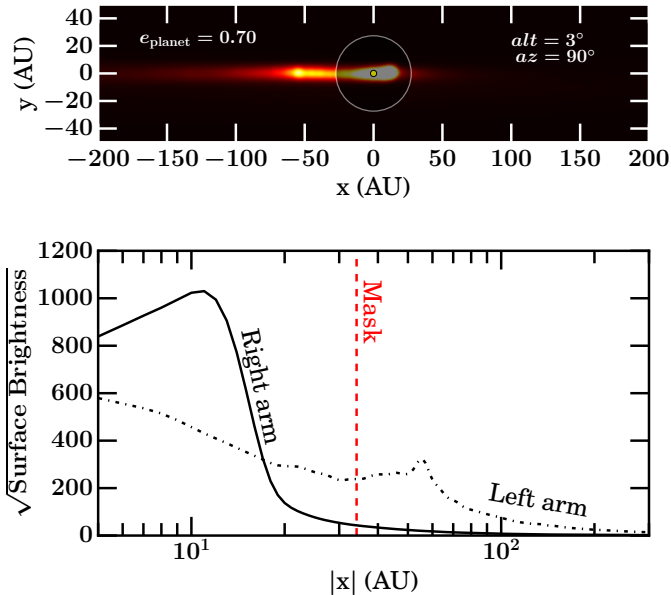


Figure 10. Zoom-in on our model “needle.” As long as the coronagraphic mask covers enough of the central cavity — specifically the region near periape, where the disk is at maximum brightness — then the disk’s longer arm can appear brighter than its shorter arm, as is consistent with observations of HD 15115. Accompanying surface brightness profiles for each arm are computed versus radius $|x|$ by integrating over y . Each profile features a local maximum where the line of sight intersects regions near the ansa of the cavity rim.

the emission farther from the star to be concave up (the latter curvature is consistent with the *HST* images from Schneider et al. 2014). We can reproduce this reversal of concavity between small and large scales by identifying the observed concave downward disk with the bright arc above the star (the apoapse of the innermost cavity rim, pointed toward the observer), and the concave upward disk with the wingtips.

A third example of a fan/moth is given by HD 15745; see, e.g., Figure 1 of Kalas et al. (2007a) and Figures 13 and 14 of Schneider et al. (2014; note the typo in the source HD number in the caption to Figure 13). Unlike the case for HD 61005 and HD 32297, isophotal ellipses describe well the fan of HD 15745, and indicate that this disk is not necessarily eccentric: an axisymmetric disk viewed somewhat above its orbital plane, composed of grains that strongly forward-scatter, can reproduce the morphology of HD 15745. See Figure 4 of Kalas et al. (2007a), or our Figure 4 (e.g., $alt = 10^\circ$).

An alternative way to produce a moth-like morphology is to allow the interstellar medium (ISM) to secularly perturb dust grain orbits (Maness et al. 2009).⁵ The mono-directional flow of the ISM across the disk can induce a global disk eccentricity and thereby mimic some of the

⁵ Secular ISM perturbations on grains that remain bound to the host star, as proposed by Maness et al. (2009), should not be confused with ISM deflections of unbound grains (Debes et al. 2009). Unbound grains contribute negligibly to disk surface brightness; compared to bound grains, unbound grains have lifetimes that are shorter by orders of magnitude, and so their relative steady-state population is correspondingly smaller (e.g., Strubbe & Chiang 2006; Krivov et al. 2006). See Maness et al. (2009, their section 4) for a detailed discussion of the various flavors of ISM interactions, including empirical arguments against interaction with a high density (~ 100 atoms per cm^3) ISM in the case of HD 61005.

effects of an eccentric planet. As Maness et al. (2009) recognize (see their section 5.1), this mechanism is subject to uncertainties in the host stellar wind; in principle, the stellar wind can blow an “astrosphere” shielding disk grains from ISM interactions.

4.3. “Bar”

A faint bar emerges when disks are viewed close to but not completely edge-on, with the embedded planet’s periape pointing out of the sky plane (bottom right panel of Figure 9). The bar, which can be $\sim 20\%$ brighter than the gap separating it from the main disk, is composed of dust grains lingering at the apastra of orbits that are nearly apsidally anti-aligned relative to the planet’s orbit. These grains are launched onto highly eccentric, barely bound orbits from the apastra of the parent body ring. Detecting the bar would confirm that the grain size distribution rises sharply toward the radiation blow-out value as a consequence of the long collisional lifetimes afforded by highly eccentric grains (Strubbe & Chiang 2006). Such a top-heavy size distribution ensures that dust orbit eccentricities cluster about a unique value; a pure Dohnanyi size distribution is actually insufficiently top heavy and does not produce bars.

4.4. “Needle”

Needles appear when eccentric and vertically thin disks are viewed edge-on with their semi-minor axes nearly parallel to the line of sight (middle left panel of Figure 9). Needles possess not only length asymmetries — one limb appears longer than the other — but also brightness asymmetries.⁶ As Figure 10 details, the shorter arm, containing dust grains crammed closer to the star, has a higher peak brightness where the line of sight runs through the periape of the ring cavity. Our model needle is reminiscent of the prototype HD 15115 (“The Blue Needle”): see, e.g., Figure 1 of Kalas et al. (2007b); Figure 11 of Schneider et al. (2014); and Figure 1 of MacGregor et al. (2015). These observations show the longer arm to be brighter than the shorter arm (cf. Figure 1 of Rodigas et al. 2012 and Figure 1 of Mazoyer et al. 2014 which show more of a brightness asymmetry than a length asymmetry). Bright long arms can be explained by our model needle provided the coronagraphic mask is large enough to block out the global maximum in surface brightness which lies along the shorter arm; see Figure 10. A prediction of the model is that beneath the mask, the surface brightness profiles of the two arms should cross, with the shorter arm ultimately outshining the longer arm sufficiently close to the star.

4.5. “Ship-and-Wake”

Akin to needles are ships and their associated wakes, which appear when eccentric parent rings, viewed edge-on and close to quadrature, have sufficiently large inclination dispersions that vertical structure can be resolved

⁶ Of course, if the parent ring is circular, or if an eccentric ring is seen exactly edge-on with its major axis parallel to the line of sight, then both limbs will appear of equal length and brightness (Figure 4, $alt = 0^\circ$). This limiting case of a “symmetric needle” may apply to AU Mic, modulo its mysterious non-axisymmetric and time-dependent clumps (Fitzgerald et al. 2007; Schneider et al. 2014; Wang et al. 2015; Boccaletti et al. 2015).

(bottom left panel of Figure 9). The ship appears on length scales of the inner cavity rim. The wake, tracing large-scale diffuse emission, is vertically thicker in the direction of the planet’s apastron.

The wake might be relevant for HD 106906. On comparatively small scales within ~ 1 arcsec (92 AU) of the star, the disk’s western arm appears shorter than its eastern arm, as resolved by the *Gemini Planet Imager* and *SPHERE* (Figure 1 of Kalas et al. 2015 and Figure 1 of Lagrange et al. 2016, respectively). We would interpret these observations to imply that the underlying planet’s periape points west. On larger scales outside ~ 2 arcsec, the *Hubble Space Telescope (HST)* reveals the nebulosity to the east to be more diffuse than to the west (Kalas et al. 2015, their Figure 3) — this is consistent with the eastern nebulosity being the back of the wake, comprising dust grains near the apastron of eccentric orbits apsidally aligned with the planet’s. A potential problem with this interpretation is that the *HST* image also evinces a radially long extension to the west, suggesting that apoapse points west instead of east. The complete picture must ultimately include HD 106906b, the substellar companion at a projected distance of ~ 7 arcsec from the star (Bailey et al. 2014). It may be that the system is not dynamically relaxed but has been perturbed by a flyby (Larwood & Kalas 2001; Kalas et al. 2015).

4.6. Future Improvements

Our model can be improved in a number of ways. A more accurate calculation of the distribution of dust grain launch sites as a function of parent body orbital phase would be welcome. We found that the appearance of “moth”-like disks depended on this distribution: if parent bodies collide preferentially near their periastra, launching more dust grains there, then the wings of the moth would be angled more sharply downward. Collision rates and grain size distributions, each a function of position, depend on one another; moreover, the entire disk is spatially interconnected, as dust grains on orbits made highly eccentric by radiation pressure can collide with particles at a range of orbital radii. Numerical simulations — e.g., *SMACK* (Nesvold et al. 2013), augmented to include radiation pressure (Nesvold & Kuchner 2015a) — can help to solve this problem.

The impact of different scattering phase functions can be explored. Our images, constructed with a single Henyey-Greenstein scattering phase function having a fixed asymmetry parameter g , can be made more realistic by accounting for how smaller grains scatter light more isotropically (smaller grains should have smaller g values than larger grains). Hedman & Stark (2015) find empirically that the light scattering properties of Saturn’s rings resemble those of irregularly shaped particles and submit them for application to debris disks.

Warps — misalignments between inner and outer disks — are missing from our models of single planets in steady-state (secularly relaxed) disks. Positing two or more planets on mutually inclined orbits produces warps (e.g., Wyatt et al. 1999). A single planet can also induce a transient warp (Mouillet et al. 1997), as has been apparently confirmed by the discovery of beta Pictoris b (Lagrange et al. 2010). See also, however, Millar-Blanchaer et al. (2015) and Apai et al. (2015) who report features in beta Pic that a single planet may be unable

to explain.

Higher-order secular effects relevant at high planet eccentricity and high inclination relative to the parent body disk (e.g., Veras & Armitage 2007; Li et al. 2014; Pearce & Wyatt 2014; Nesvold et al. 2016), and explicit numerical tests of dynamical stability, can also be incorporated in future models. Other neglected dynamical effects include those from non-overlapping mean-motion resonances (e.g., Kuchner & Holman 2003; Stark & Kuchner 2009). Observational evidence for the relevance of individual MMRs is so far scant except for among Kuiper belt objects (e.g., Batygin & Brown 2016; Volk et al. 2016) and in the inner Solar System’s zodiacal dust disk (e.g., Dermott et al. 1994; Reach 2010; Jones et al. 2013).

We thank Gaspard Duchêne, Tom Esposito, Mike Fitzgerald, James Graham, Paul Kalas, Max Millar-Blanchaer, Ruth Murray-Clay, Erika Nesvold, Chris Stark, and Jason Wang for encouraging and insightful discussions, and prompt and constructive feedback on a draft version of this manuscript. An anonymous referee provided a helpful and exceptionally fast report. EJL is supported in part by the Natural Sciences and Engineering Research Council of Canada under PGS D3 and the Berkeley Fellowship. EC acknowledges support from grants AST-0909210 and AST-1411954 awarded by the National Science Foundation, and NASA Origins grant NNX13AI57G. This research used the Savio computational cluster resource provided by the Berkeley Research Computing program at the University of California, Berkeley (supported by the UC Berkeley Chancellor, Vice Chancellor of Research, and the Chief Information Officer).

REFERENCES

- Apai, D., Schneider, G., Grady, C. A., et al. 2015, *ApJ*, 800, 136
 Bailey, V., Meshkat, T., Reiter, M., et al. 2014, *ApJ*, 780, L4
 Batygin, K., & Brown, M. E. 2016, *AJ*, 151, 22
 Beuzit, J.-L., Feldt, M., Dohlen, K., et al. 2008, in *Proc. SPIE*, Vol. 7014, Ground-based and Airborne Instrumentation for Astronomy II, 701418
 Boccaletti, A., Thalmann, C., Lagrange, A.-M., et al. 2015, *Nature*, 526, 230
 Buenzli, E., Thalmann, C., Vigan, A., et al. 2010, *A&A*, 524, L1
 Chiang, E., Kite, E., Kalas, P., Graham, J. R., & Clampin, M. 2009, *ApJ*, 693, 734
 Currie, T., Rodigas, T. J., Debes, J., et al. 2012, *ApJ*, 757, 28
 Debes, J. H., Weinberger, A. J., & Kuchner, M. J. 2009, *ApJ*, 702, 318
 Dermott, S. F., Jayaraman, S., Xu, Y. L., Gustafson, B. Å. S., & Liou, J. C. 1994, *Nature*, 369, 719
 Esposito, T. M., Fitzgerald, M. P., Graham, J. R., & Kalas, P. 2014, *ApJ*, 780, 25
 Fitzgerald, M. P., Kalas, P., & Graham, J. R. 2011, in *AAS/Division for Extreme Solar Systems Abstracts*, Vol. 2, AAS/Division for Extreme Solar Systems Abstracts, 7.06
 Fitzgerald, M. P., Kalas, P. G., Duchêne, G., Pinte, C., & Graham, J. R. 2007, *ApJ*, 670, 536
 Grady, C. A., Schneider, G., Carson, J., et al. 2016, in *American Astronomical Society Meeting Abstracts*, Vol. 227, American Astronomical Society Meeting Abstracts, 343.10
 Heap, S. R., Lindler, D. J., Lanz, T. M., et al. 2000, *ApJ*, 539, 435
 Hedman, M. M., & Stark, C. C. 2015, *ApJ*, 811, 67
 Hines, D. C., Schneider, G., Hollenbach, D., et al. 2007, *ApJ*, 671, L165
 Hughes, A. M., Wilner, D. J., Mason, B., et al. 2012, *ApJ*, 750, 82
 Jalali, M. A., & Tremaine, S. 2012, *MNRAS*, 421, 2368
 Jones, M. H., Bewsher, D., & Brown, D. S. 2013, *Science*, 342, 960

- Jovanovic, N., Martinache, F., Guyon, O., et al. 2015, *PASP*, 127, 890
- Kalas, P., Duchene, G., Fitzgerald, M. P., & Graham, J. R. 2007a, *ApJ*, 671, L161
- Kalas, P., Fitzgerald, M. P., & Graham, J. R. 2007b, *ApJ*, 661, L85
- Kalas, P., Graham, J. R., & Clampin, M. 2005, *Nature*, 435, 1067
- Kalas, P. G., Rajan, A., Wang, J. J., et al. 2015, *ApJ*, 814, 32
- Krivov, A. V., Löhne, T., & Sremčević, M. 2006, *A&A*, 455, 509
- Kuchner, M. J., & Holman, M. J. 2003, *ApJ*, 588, 1110
- Lagrange, A.-M., Bonnefoy, M., Chauvin, G., et al. 2010, *Science*, 329, 57
- Lagrange, A.-M., Langlois, M., Gratton, R., et al. 2016, *A&A*, 586, L8
- Larwood, J. D., & Kalas, P. G. 2001, *MNRAS*, 323, 402
- Li, G., Naoz, S., Kocsis, B., & Loeb, A. 2014, *ApJ*, 785, 116
- MacGregor, M. A., Wilner, D. J., Andrews, S. M., & Hughes, A. M. 2015, *ApJ*, 801, 59
- Macintosh, B., Graham, J. R., Ingraham, P., et al. 2014, *Proceedings of the National Academy of Science*, 111, 12661
- Maness, H. L., Kalas, P., Peek, K. M. G., et al. 2009, *ApJ*, 707, 1098
- Mazoyer, J., Boccaletti, A., Augereau, J.-C., et al. 2014, *A&A*, 569, A29
- Millar-Blanchaer, M. A., Graham, J. R., Pueyo, L., et al. 2015, *ApJ*, 811, 18
- Mouillet, D., Larwood, J. D., Papaloizou, J. C. B., & Lagrange, A. M. 1997, *MNRAS*, 292, 896
- Murray, C. D., & Dermott, S. F. 2000, *Solar System Dynamics* ("Cambridge University Press")
- Nesvold, E. R., & Kuchner, M. J. 2015a, *ApJ*, 815, 61
- . 2015b, *ApJ*, 798, 83
- Nesvold, E. R., Kuchner, M. J., Rein, H., & Pan, M. 2013, *ApJ*, 777, 144
- Nesvold, E. R., Naoz, S., Vican, L., & Farr, W. M. 2016, *ArXiv e-prints*, arXiv:1603.08005
- Padgett, D., & Stapelfeldt, K. 2016, in *IAU Symposium*, Vol. 314, *IAU Symposium*, ed. J. H. Kastner, B. Stelzer, & S. A. Metchev, 175–178
- Pan, M., & Schlichting, H. E. 2012, *ApJ*, 747, 113
- Pearce, T. D., & Wyatt, M. C. 2014, *MNRAS*, 443, 2541
- Perrin, M. D., Duchene, G., Millar-Blanchaer, M., et al. 2015, *ApJ*, 799, 182
- Quillen, A. C. 2006, *MNRAS*, 372, L14
- Quillen, A. C., & Faber, P. 2006, *MNRAS*, 373, 1245
- Reach, W. T. 2010, *Icarus*, 209, 848
- Ricarte, A., Moldvai, N., Hughes, A. M., et al. 2013, *ApJ*, 774, 80
- Rodigas, T. J., Malhotra, R., & Hinz, P. M. 2014, *ApJ*, 780, 65
- Rodigas, T. J., Hinz, P. M., Leisenring, J., et al. 2012, *ApJ*, 752, 57
- Schneider, G., Weinberger, A. J., Becklin, E. E., Debes, J. H., & Smith, B. A. 2009, *AJ*, 137, 53
- Schneider, G., Grady, C. A., Hines, D. C., et al. 2014, *AJ*, 148, 59
- Shannon, A., & Wu, Y. 2011, *ApJ*, 739, 36
- Stark, C. C., & Kuchner, M. J. 2009, *ApJ*, 707, 543
- Strubbe, L. E., & Chiang, E. I. 2006, *ApJ*, 648, 652
- Thalmann, C., Janson, M., Buenzli, E., et al. 2011, *ApJ*, 743, L6
- Veras, D., & Armitage, P. J. 2007, *ApJ*, 661, 1311
- Volk, K., Murray-Clay, R., Gladman, B., et al. 2016, *ArXiv e-prints*, arXiv:1604.08177
- Wahhaj, Z., Liu, M. C., Biller, B. A., et al. 2014, *A&A*, 567, A34
- Wang, J. J., Graham, J. R., Pueyo, L., et al. 2015, *ApJ*, 811, L19
- Wisdom, J. 1980, *AJ*, 85, 1122
- Wyatt, M. C. 2008, *ARA&A*, 46, 339
- Wyatt, M. C., Dermott, S. F., Telesco, C. M., et al. 1999, *ApJ*, 527, 918